

InfraRed Investigation in Singapore (IRIS) Observatory: Urban heat island contributors and mitigators analysis using neighborhood-scale thermal imaging

Miguel Martin¹, Vasantha Ramani¹, Clayton Miller^{2,*}

¹Berkeley Education Alliance for Research in Singapore, Singapore

²College of Design and Engineering, National University of Singapore (NUS), Singapore

*Corresponding Author: clayton@nus.edu.sg, +65 81602452

Abstract

This paper studies heat fluxes from contributors and mitigators of urban heat islands using thermal images and weather data. Thermal images were collected from an observatory operating on the rooftop of a building between November 2021 and April 2022. Over the same period, an automatic weather station network was used to measure weather conditions at several locations on a university campus in Singapore. From data collected by the observatory and the automatic weather station network, a method was developed to estimate the heat emitted by building façades, vegetation, and traffic. Before performing the analysis of urban heat fluxes, it was observed that the surface temperature collected from the observatory is sensitive to some variables. After the sensitivity analysis, thermal images were calibrated against measurements of the surface temperature in an outdoor environment. Finally, several contributors and mitigators of urban heat islands were analyzed from heat fluxes assessed with thermal images and weather data. According to thermal images collected by the rooftop observatory, concrete walls are an important contributor to urban heat islands due to the longwave radiation they emit at night. Vegetation, on the other hand, seems to be an effective mitigator because of latent heat fluxes generated by evapotranspiration. Traffic looks to be a negligible source of heat if considered over a small portion of a road. In the future, more efforts can be made to estimate the magnitude of the heat released by an air-conditioning system from thermal images.

Keywords: Urban heat island, Infrared thermography, Automatic weather stations, Building façades, Vegetation, Traffic

Nomenclature

ε	Thermal emissivity	0-1
ω	Water vapour content	kg _{water} /kg _{air}
ϕ	Relative humidity	0-1 or %
ρ	Density	kg/m ³
σ	Stefan-boltzmann constant ($5.67 \cdot 10^{-8}$)	W/m ² -K ⁴
τ	Solar transmissivity	0-1
A	Area	m ²
c_p	Specific heat	J/kg-K
c_{veg}	Specific heat of vegetation	J/m ² -K
E_{fuel}	Fuel consumption	J/m
e	Water vapour pressure	hPa
h	Convective heat transfer coefficient	W/m ² -K
K	Shortwave radiation	W/m ²
k	Thermal conductivity	W/m-K
L	Longwave radiation	W/m ²
LAI	Leaf Area Index	m ² /m ²
l	Length	m
N	Number of	-
Q	Heat flux	W/m ²
r_a	Aerodynamic resistance	s/m
r_s	Stomatal resistance	s/m
T	Temperature	°C or K
t	Time	s
U	Camera output voltage	V
V	Volume	m ³

W_s Wind speed m/s
 Δx Thickness m

List of abbreviations

AWSN	Automatic Weather Station Network
HVAC	Heat, Ventilation, and Air-Conditioning
LST	Land Surface Temperature
MBE	Mean Bias Error
RMSE	Root Mean Square Error
UHI	Urban Heat Island

1. Introduction

Nowadays, more than half of the world's population lives in cities [1]. To accommodate these agglomerations of inhabitants, buildings and streets have been constructed in large quantities. The expansion of built-up surfaces is a major cause of Urban Heat Island (UHIs), together with the absence of vegetation and the augmentation of human activity. UHIs are responsible for heat stress in various cities around the world, and thus, it is perceived as a threat to public health and urban sustainability [2]. Due to the importance of this climatic phenomenon, various methods have been studied to monitor UHIs in cities [3].

One of the oldest methods consists of observing UHIs from thermal images collected by satellites. In 1979, [4] published a thermal image obtained from a satellite on top of New York

City. At that time, it was only possible to qualitatively compare the Land Surface Temperature (LST) of a city with this of its rural surroundings. It was only in the 1990s that a quantitative assessment of UHIs could be made from satellite images. For example, [5] assessed the LST difference between urban and rural areas of Vancouver and Los Angeles from thermal images collected from NOAA-7, -8, and -9 satellites. Despite this major improvement, the resolution with which UHIs can be monitored remains limited. Since the 2000s, the resolution of thermal images collected by satellites has been enhanced due to significant advancements in infrared thermography. Among the most recent uses of thermal images collected by a satellite, there is the study conducted by [6] in which the UHI of Shenzhen city (China) was assessed with a high resolution.

Thermal images collected from a satellite can only be used to observe the impact of urbanization on the LST, that is, the surface UHI. To understand the effect of urban areas on the air temperature at the street level, other studies have collected data from an Automatic Weather Station Network (AWSN). As shown in [7], an AWSN consists of several weather stations installed at different positions of a city and its suburban or rural surroundings. Among weather conditions recorded by each station, the outdoor air temperature is the one which is the most commonly used to observe UHIs [8, 9, 10, 11, 12, 13, 14]. Nevertheless, other weather conditions measured by an AWSN are worth to be considered, in particular when studying the impact of urbanization on outdoor thermal comfort [15, 16, 17, 18]. In comparison with measurements obtained from a satellite, these collected from an AWSN have a higher temporal resolution but a lower spatial resolution.

To improve the spatial resolution with which the outdoor air temperature is observed from an AWSN, various interpolation methods have been used in the literature [19, 20, 21, 22, 23, 24, 25, 26, 27]. Estimates provided by these interpolation methods are relatively accurate at positions near weather stations. However, at positions in between two or more weather stations, their accuracy decreases significantly. This loss in accuracy is explained by the fact that UHIs is a complex and highly dynamic phenomenon that cannot fully be observed by interpolating the outdoor temperature obtained from an AWSN.

Since the 2010s, several studies have attempted to improve the resolution and the accuracy with which the outdoor air temperature of a city can be observed using data obtained from a satellite as an input of a statistical model. Most statistical models consider the LST and the portion of vegetation as an input [28, 29, 30, 31, 32, 33, 34, 35]. Others rely on the topography and/or the land use assessed from satellite images [36, 37, 38, 39, 40]. Although these statistical models seem to provide appropriate observations of the UHI, they can hardly be used to determine how buildings contribute to its exacerbation and vegetation to its mitigation.

To monitor the influence of buildings and vegetation on UHIs at the city scale, it is possible to assess urban heat fluxes from remotely sensed data obtained from a satellite and weather conditions collected by an AWSN. Data obtained from a satellite are particularly useful for estimating the net-all wave radiation [41, 42, 43, 44, 45, 46, 47, 48]. If combined with weather

data, they can be used to assess sensible and/or latent heat fluxes [49, 50, 51, 52]. The net-all wave radiation, the sensible heat flux, and the latent heat flux can be balanced to estimate the anthropogenic heat releases and/or the net-heat storage [53, 54, 55, 56, 57, 58]. Some studies also included the net-advection in the urban energy balance but often consider it negligible [59, 60, 61].

So far, urban heat fluxes have essentially been studied at the city scale; and thus, little is known at the neighborhood scale. Among the few studies conducted at the neighborhood scale, [62] and Morrison et al. [63, 64] assessed the longwave radiation emitted by several urban facets from an observatory. An observatory was also used by [65] to estimate the sensible heat transferred by buildings in Hong Kong (China) to the outdoor air. By sensible heat, it is here referred to as the total heat transferred by convection and radiation over a period. In other studies, like [66], the sensible heat corresponds to the heat which is exclusively transferred by convection at a specific time, that is, the convective or sensible heat flux. Instead of the sensible heat flux, [67] tried to detect the anthropogenic heat emitted by a heating, ventilation, and air-conditioning (HVAC) systems at the neighborhood scale. While these studies provide some clues on contributors to UHIs at the neighborhood scale, they have not considered elements that might act as mitigators like vegetation. In addition, they have not made any observation on the heat emitted by traffic using thermal images.

This study aims to fill this gap by showing that thermal images, together with weather data collected by an AWSN, can help in analyzing the heat emitted by contributors and mitigators to UHIs at the neighborhood scale. This research objective was achieved by: 1) Defining a method to calculate heat fluxes from building façades, vegetation, and traffic using thermal images and weather data, 2) Recording thermal images of several buildings and green areas from a rooftop observatory, and 3) Collecting weather data at different positions from an AWSN. From the results of this study, the scientific community would have a better understanding of the reasons why some elements in an urban area considerably contribute to UHIs, while others can mitigate it. The results would also help urban planners determine how more sustainable and comfortable cities can be developed in the future.

The method used to analyze urban heat fluxes at the neighborhood scale is described in Section 2. It comprises the mathematical formulation of urban heat fluxes, the description of experimental instruments, and the explanation of the sensitivity analysis and validation. In Section 3, the results of this study are detailed and discussed. Finally, conclusions are explained in Section 4.

2. Materials and Methods

2.1. Definition of heat fluxes

Any built-up surface in an urban area absorbs and emits heat in accordance with the following energy balance:

$$Q^* = Q_H + Q_G + \Delta Q_S \quad (1)$$

Q^* corresponds to the net-all wave radiation; that is, the heat gained or lost by radiation in the short- and longwave range.

Mathematically, it is defined from the shortwave radiation emitted by the sun on the surface (K^\downarrow), the longwave radiation emitted by surroundings on the surface (L^\downarrow), the portion of shortwave radiation reflected by the surface (K^\uparrow), and the longwave radiation emitted by the surface (L^\uparrow) as:

$$Q^* = K^\downarrow + K^\uparrow + L^\downarrow + L^\uparrow \quad (2)$$

At night, the net-shortwave radiation ($K^* = K^\downarrow + K^\uparrow$) is negligible; and thus, the energy balance can be expressed as:

$$L^* = Q_H + Q_G + \Delta Q_S \quad (3)$$

where $L^* = L^\downarrow + L^\uparrow$ is the net-longwave radiation. It can be directly calculated using the following formula:

$$L^* = \varepsilon\sigma F_{sky} (T_{sky}^4 - T_S^4) + \varepsilon\sigma \sum_{S' \in \mathcal{N}_S} F_{S \rightarrow S'} (T_{S'}^4 - T_S^4) \quad (4)$$

where T_{sky} is the sky temperature, ε the emissivity of the surface, F_{sky} its sky view factor, \mathcal{N}_S the set of its surrounding surfaces in the urban area, $F_{S \rightarrow S'}$ its view factor with one of the surrounding surface, and $T_{S'}$ the temperature of one of its surrounding surface. Due to the difficulty in directly evaluating L^* from Equation 4 using thermal images, it is usually recommended to indirectly assess it from Q_H , Q_G , and ΔQ_S . Q_H corresponds to the heat transferred from the surface to the outdoor air by convection. It is often referred as the sensible heat flux and expressed as:

$$Q_H = h(T_S - T_{air}) \quad (5)$$

where h is the convective heat transfer coefficient between the surface and the outdoor air and T_{air} the outdoor air temperature. While T_{air} can be directly obtained from an AWSN, T_S needs to be assessed from a thermal image as:

$$T_S = \frac{1}{|\mathcal{S}|} \sum_{ij \in \mathcal{S}} T_{ij} \quad (6)$$

where \mathcal{S} referring to the set of all Positions ij in the thermal image that correspond to the surface, and T_{ij} the temperature at Position ij of the thermal image. There are various methods to evaluate h , but one of the simplest is to use an empirical relation with respect to wind speed W_s measured from an AWSN, that is:

$$h = b + a \cdot W_s^c \quad (7)$$

For instance, [68] considered that $a = 4.2$, $b = 11.8$, and $c = 1$ for all built-up surfaces inside the urban canopy. Similarly to Q_H , the net heat stored by a surface (ΔQ_S) can be directly estimated from T_S as:

$$\Delta Q_S = \Delta x \rho c_p \frac{\Delta T_S}{\Delta t} \quad (8)$$

where $\Delta T_S / \Delta t$ is the rate of temperature change of the surface, Δx its thickness, ρ its density, and c_p its specific heat capacity. Finally, the heat transfer from the outer to the inner layer of the surface by conduction (Q_G) can be obtained using the Fourier first law of heat conduction, that is:

$$Q_G = \frac{k}{\Delta x} (T_S - T_{S_{in}}) \quad (9)$$

where k is the thermal conductivity of the surface, and $T_{S_{in}}$ the inner layer temperature.

Equation 10 is valid for opaque surfaces; that is surfaces absorbing and reflecting incoming solar radiation (K^\downarrow). Transparent surfaces also transmit a portion τ of K^\downarrow into buildings. It means that their energy balance is expressed as:

$$Q^* - \tau K^\downarrow = Q_H + Q_G + \Delta Q_S \quad (10)$$

where τK^\downarrow is the transmitted incoming solar radiation through the transparent surface.

In their vegetated urban canopy model, [69] expressed the heat absorbed and emitted by vegetation as:

$$Q^* = Q_H + Q_E + \Delta Q_S \quad (11)$$

where Q_E is the latent heat flux produced by evapotranspiration. Using the formulation of [60], Q_E can be estimated from thermal images and an AWSN as:

$$Q_E = \frac{\rho c_p}{\gamma} \left(\frac{e_S^*(T_S) - e_{air}}{r_a + r_s} \right) \quad (12)$$

where ρ is the density of the outdoor air, c_p its specific heat, γ a constant ($= 0.67$ hPa/K), $e_S^*(T_S)$ the saturated vapour pressure at temperature T_S of the vegetation, e_{air} the water pressure of the outdoor air, r_a the aerodynamic resistance between the vegetation and the outdoor air, and r_s the stomatal resistance. Instead of using the log-law, r_a can be expressed from h as:

$$r_a = \rho c_p / h \quad (13)$$

r_s depends on the outdoor air temperature and the downward shortwave radiation, which can be assessed from measurements of an AWSN. The outdoor air temperature and relative humidity measured by the AWSN can be used to evaluate e_{out} . The net-all wave radiation (Q^*) and the sensible heat flux (Q_H) of the vegetation can be calculated as in Equations 2 and 5, respectively. However, the net-heat stored by the vegetation (ΔQ_S) needs to be calculated as:

$$\Delta Q_S = c_{veg} \frac{\Delta T_S}{\Delta t} \quad (14)$$

where c_{veg} is the heat capacitance of the vegetation. According to [69], c_{veg} can be expressed as:

$$c_{veg} = 4186 \cdot LAI \quad (15)$$

where LAI is the leaf area index.

In addition to the heat emitted by built-up surfaces and vegetation, it's important to consider anthropogenic heat releases (Q_F) when studying UHIs at the neighborhood scale. Q_F is a combination of heat fluxes that primarily originate from HVAC systems of buildings Q_{HVAC} and traffic $Q_{traffic}$, that is:

$$Q_F = Q_{HVAC} + Q_{traffic} \quad (16)$$

[67] shows that waste heat releases (Q_{HVAC}) can be detected from thermal images. However, their magnitude can only be estimated if measurements of the building energy use are available [70]. In contrast with Q_{HVAC} , $Q_{traffic}$ can be estimated from

thermal images without needing any additional data source. The reason is that the number of cars crossing a portion of the road at an instant n (N_v^n) can be detected from thermal images taken at two subsequent times. It means there is a function f such that:

$$f(|U_{\mathcal{R}}^{n+1} - U_{\mathcal{R}}^n|) = N_v^n \quad (17)$$

where $U_{\mathcal{R}}^n = U_{\mathcal{R}}^n - \langle U_{\mathcal{R}}^n \rangle$ is the thermal image within the region \mathcal{R} taken at time $t_0 + n \cdot \Delta t$ and centered over the average $\langle U_{\mathcal{R}}^n \rangle$. Given f , the number of vehicles crossing the portion of the road \mathcal{R} over one hour from time t (N_v) can be calculated as:

$$N_v = \sum_{n=(t-t_0)/\Delta t}^{(t+3600-t_0)/\Delta t} N_v^n = \sum_{n=(t-t_0)/\Delta t}^{(t+3600-t_0)/\Delta t} f(|U_{\mathcal{R}}^{n+1} - U_{\mathcal{R}}^n|) \quad (18)$$

Thus, Q_{traffic} can be defined from the expression of [71], that is:

$$Q_{\text{traffic}} = \frac{1}{3600 \cdot A_{\text{road}}} (N_v \cdot l_{\text{road}} \cdot E_{\text{fuel}}) \quad (19)$$

where A_{road} is the area of the portion of road corresponding to the region \mathcal{R} , l_{road} its length, and E_{fuel} the fuel consumption per car.

2.2. Rooftop observatory

From November 2021 to March 2022, an observatory was operating at the rooftop level to collect thermal images of different buildings on a university campus in Singapore. Singapore is a city-state in South-East Asia located near the equator. At this location, a hot and humid climate is experienced over the year. The air temperature varies between 26 and 30 degrees Celsius on average every month. The monthly average humidity is also relatively constant, with variations between 80 and 90 percent. When not obstructed by buildings, the wind blows at a speed between 1 and 4 meters per second from the South-East direction on average every month at the ground level.

The observatory was installed on the rooftop of a 42-meter-tall building located in a residential area, as illustrated in Figure 1. The residential area is located in front of a university campus consisting of office and educational buildings. Among the buildings, four can be observed from the observatory with a proper resolution. Building A is one of the tallest on the university campus. It is about 68-meter-tall with an important portion of its façade covered by curtain walls. Closer to the observatory are Buildings B and C, which are both about 27-meter-tall. Their façade consists of concrete walls and single-pane windows. In addition to concrete walls, the façade of Building D consists of metal grids installed on a concrete frame. Building D was designed to be net-zero, and its height is around 24 meters. Around buildings A, B, C, and D, it is possible to observe several tropical trees from the observatory. In front of buildings B, C, and D, there is a road with heavy traffic.

On the top of the observatory, there is a housing containing a FLIR A300 (9Hz) thermal camera as described in Table 1. The housing enables the thermal camera to be protected against heavy rains with IP67 protection. It was fixed on a pan/tilt unit in order to record thermal images at different positions. To avoid any obstacles while recording thermal images, the pan/tilt unit,

together with the housing, including the thermal camera, was placed on a 2-meter-high truss tower. This structure is stabilized by concrete blocks and protected against lightning by an air terminal. On the truss tower, two sockets were installed to power up the thermal camera and the direct current motor of the pan/tilt unit from a backup battery located in a water tank room. The backup battery is continuously recharged from the electrical source of the building so as to keep the thermal camera and the pan/tilt unit operating for up to 2 hours in case of power shutdown. The thermal camera and the pan/tilt unit were also connected to a laptop for configuring and checking the collection of thermal images.

The collection of thermal images was configured from two separate software. One software was installed on a video encoder to command the pan/tilt unit. From its graphical interface, it is possible to define the positions where the pan/tilt unit must stop to take a thermal image. The moment when a thermal image is taken is controlled by another software installed on the laptop. Thermal images can be saved either in JPEG or FFF file format inside a folder to be specified in the software.

The thermal camera and the pan/tilt unit were configured so that images can be taken at four positions, as shown in Figure 2. Position I is centered on Building A. From this position, it is also possible to observe vegetation consisting of tropical trees mostly. After staying at Position I for a while, the observatory moves to Position II. This position primarily focuses on Building B and its surrounding vegetation. A similar thermal image is taken at Position III but centered on Building D. Finally, the observatory stops at Position IV where various elements can be observed, including Building D, vegetation, and a road. For each position, thermal images are recorded at a rate of one minute approximately. They are stored on a Google Drive repository through a 4G Internet connection installed on the laptop.

Regardless of whether thermal images are saved in JPEG or FFF, they contain a header and an array U_{ij}^r corresponding to the output voltage measured by the infrared receptor at position ij of the thermal image. U_{ij}^r can be converted into longwave radiations between 7.5 and 13 micrometers (L_{ij}^r) using the following expression:

$$U_{ij}^r = c L_{ij}^r \quad (20)$$

where c is a constant. The FLIR A300 (9Hz) thermal camera installed in the observatory was calibrated so that the surface temperature of a target element measured by the infrared receptor (T_{ij}^r) satisfies the following relation:

$$T_{ij}^r = g(U_{ij}^r) = b \ln \left[\frac{r_1}{r_2 (U_{ij}^r + O)} + f \right]^{-1} \quad (21)$$

where b , r_1 , r_2 , O , and f are calibrated parameters. It is important to note that these parameters are obtained in a controlled environment where the true surface temperature of a target element at position ij of the thermal image (T_{ij}) is almost equal to T_{ij}^r . In an outdoor environment, however, a significant discrepancy can be observed between T_{ij} and T_{ij}^r . To minimise the discrepancy T_{ij} and T_{ij}^r in an outdoor environment, parameters

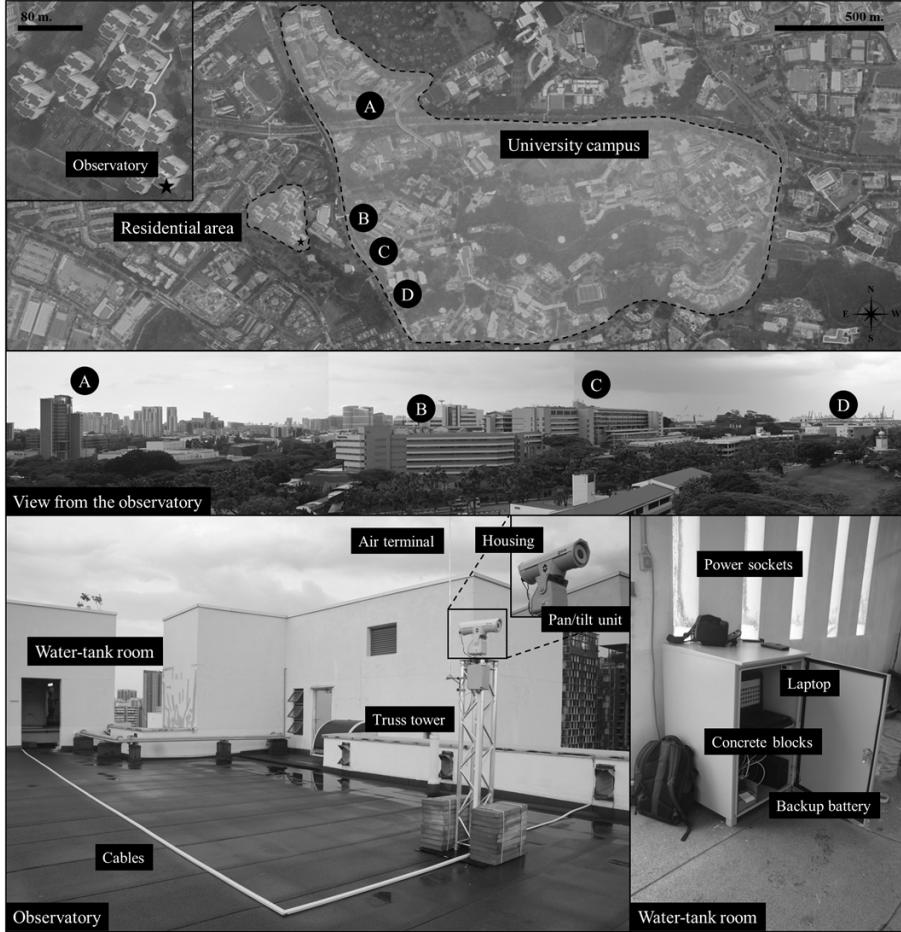


Figure 1: Observatory installed in the university campus in Singapore

Feature	Value
Field of view	25° (H) x 18.8° (V)
Image resolution	320 (H) x 240 (V) pixels
Accuracy	±2 °C or 2% of readings
Operating temperature range	-15 ... 50 °C
Storage temperature range	-20 ... 120 °C
Spectral range	7.5 ... 13 μ m
Image format	16-bit

Table 1: Specifications of the FLIR A300 (9Hz) thermal camera.

in Equation 21 usually need to be re-calibrated as explained in Section 2.5.

Apart from parameters to be calibrated, several aspects had to be considered when evaluating T_{ij} from the rooftop observatory. The first aspect is that buildings, streets, and trees observed from the observatory are exposed to longwave radiations, which mainly come from the skydome. The longwave radiation from the sky (L^{sky}) is then reflected into the air in parallel to the longwave radiation emitted by the element observed from the observatory (L). Both L^{sky} and L travel over the atmosphere before reaching the observatory. When reaching the observatory, the longwave radiation emitted by the atmosphere (L^{atm}), together with L^{sky} and L , are transmitted through the window of

the housing before being captured by the infrared receptor. The infrared receptor also receives the longwave radiation from the window (L^{win}) in addition to others.

Considering the relation expressed in Equation 20 and the aforementioned aspects, the camera output voltage corresponding to L_{ij} (U_{ij}) can be formulated as:

$$U_{ij} = \frac{1}{\varepsilon_{ij}\tau_{ij}^{atm}\tau^{win}}U_{ij}^r - \frac{1 - \varepsilon_{ij}}{\varepsilon_{ij}}U^{sky} - \frac{1 - \tau_{ij}^{atm}}{\varepsilon_{ij}\tau_{ij}^{atm}}U^{atm} - \frac{1 - \tau^{win}}{\varepsilon_{ij}\tau_{ij}^{atm}\tau^{win}}U^{win} \quad (22)$$

where ε_{ij}^m is the thermal emissivity an element at position ij in the thermal image, τ_{ij}^{atm} the transmissivity of the atmosphere between the element and the rooftop observatory, and τ^{win} the

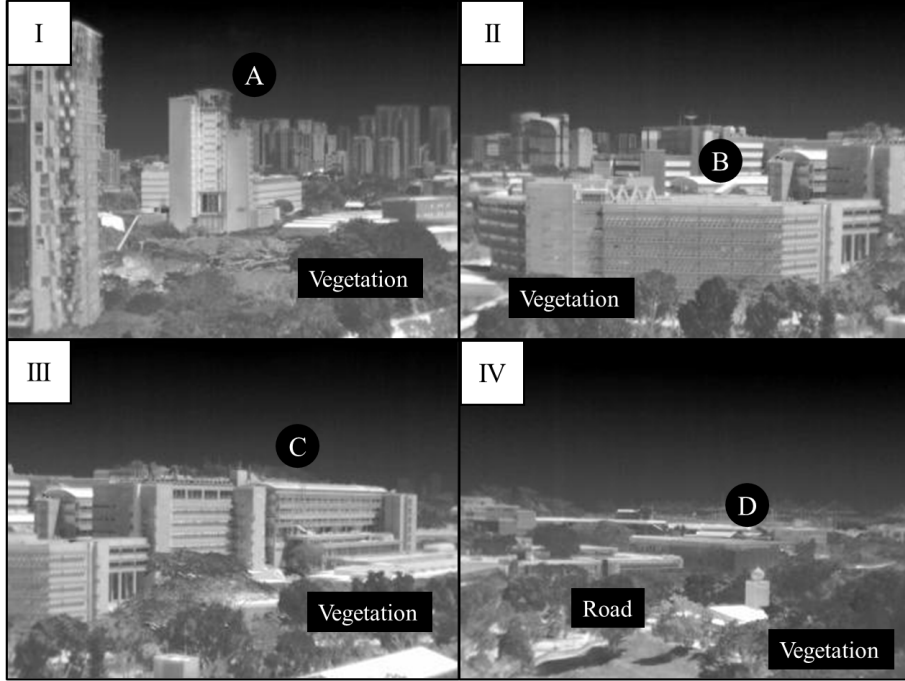


Figure 2: Positions where thermal images were recorded by the observatory.

transmissivity of the window. Knowing U_{ij} , T_{ij} can be assessed using Equation 21. While ε_{ij} and τ^{win} can be estimated from material properties of the element and the window, respectively, τ_{ij}^{atm} needs to be calculated from data collected by an AWSN.

2.3. Network of automatic weather stations

Figure 3 shows the AWNS that was used to estimate urban heat flux together with thermal images recorded by the rooftop observatory. The AWNS was deployed by [72] in February 2019. It consists of 12 weather stations measuring the air temperature and relative humidity. All stations, except 12, measure the wind speed and direction. Solar radiation is measured by all stations apart from 11 and 12. Specifications of each weather station can be found in [72].

Weather Station 1 was used to calculate τ_{ij}^{atm} as in [73], that is:

$$\tau_{ij}^{atm} = x \cdot \exp \left[-\sqrt{d_{ij}} (\alpha_1 + \beta_1 \sqrt{\omega}) \right] + (1-x) \cdot \exp \left[-\sqrt{d_{ij}} (\alpha_2 + \beta_2 \sqrt{\omega}) \right] \quad (23)$$

where d_{ij} is the distance between an element and the observatory at position ij of the thermal image, ω is the water vapour content in the atmosphere, x , α_1 , β_1 , α_2 , and β_2 empirical coefficients. ω can be estimated from the air temperature (T_{air}) and relative humidity (ϕ) measured from the weather station as:

$$\omega = \phi \cdot \exp \left[c_0 + c_1 T_{air} + c_2 T_{air}^2 + c_3 T_{air}^3 \right] \quad (24)$$

where c_0 , c_1 , c_2 , and c_3 is another set of empirical coefficients described in [73].

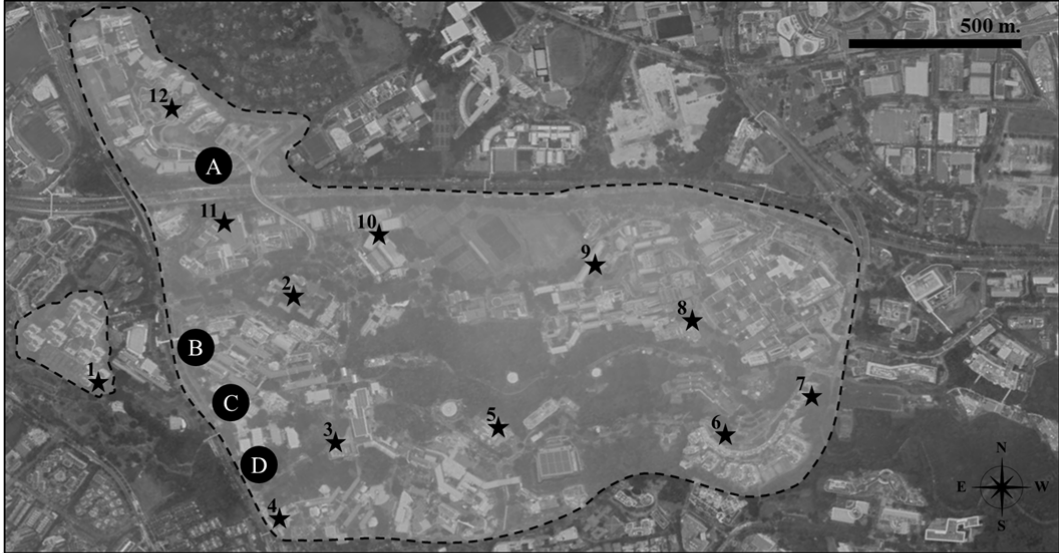
As mentioned in Section 2.1, various weather conditions measured by the AWSN need to be used for estimating the sensible and latent heat flux. For instance, sensible and latent heat fluxes

emitted by buildings and vegetation observed at Position I was assessed from the temperature, relative humidity, and wind speed as measured by the Weather Station 12. Latent heat fluxes emitted by vegetation also depend on the solar radiation, which was defined from measurements of the Weather Station 2. Measurements obtained from the Weather Station 2 were used to evaluate sensible and latent heat fluxes observed at Position II. Heat fluxes observed at Position III and IV were estimated from weather conditions measured by Weather Stations 3 and 5, respectively.

2.4. Sensitivity analysis

Before assessing T_{ij} from the observatory, a sensitivity analysis was conducted on variables that might considerably affect its variance. The contribution of a variable to the variance of T_{ij} was estimated from the first-order Sobol index [74]. The higher the first-order index of a variable is, the more T_{ij} is sensitive to that variable. However, the first order index does not consider interactions that one variable might have with others. For this reason, the total Sobol index was also calculated during the sensitivity analysis of T_{ij} .

Table 2 illustrate the variables considered during the sensitivity analysis of T_{ij} and their respective boundaries. According to [75], ε_{ij} varies between 0.8 and 1.0 in the built environment. In case ε_{ij} is slightly below 0.8, it was decided to calculate its sensitivity in a range between 0.7 and 1.0. The sky temperature ($T^{sky} = g(U^{sky})$) was measured by [76] in Singapore, and varies between 11 and 33 degrees Celsius. Based on weather data recorded by the Meteorological Service of Singapore [77], T_{air} can change between 19 and 37 degrees Celsius. ϕ is comprised between 30 and 100 percent. Using Google Earth, it was assessed that elements being observed from the thermal camera are located at a distance d_{ij} between 100 and 1000 meters. The



ID	Air temperature (in °C)	Rel. humidity (in %)	Wind speed (in m/s)	Wind direction (in Degree)	Solar radiation (in W/m²)
1	✓	✓	✓	✓	✓
2	✓	✓	✓	✓	✓
3	✓	✓	✓	✓	✓
4	✓	✓	✓	✓	✓
5	✓	✓	✓	✓	✓
6	✓	✓	✓	✓	✓
7	✓	✓	✓	✓	✓
8	✓	✓	✓	✓	✓
9	✓	✓	✓	✓	✓
10	✓	✓	✓	✓	
11	✓	✓	✓		
12	✓	✓	✓		

Figure 3: AWNS installed in a university campus by [72].

surface temperature of the window ($T^{win} = g(U^{win})$), as well as its range of values, was measured from a HOBO UX100-014M sensor. A range between 0.8 and 1.0 was considered for τ^{win} .

Variable	Min. value	Max. value
Thermal emissivity (0-1)	0.7	1.0
Sky temperature (in °C)	11.0	33.0
Air temperature (in °C)	19.0	37.0
Air relative humidity (in %)	30.0	100.0
Distance object (in m)	100.0	1000.0
Window temperature (in °C)	20.0	60.0
Window transmittance (0-1)	0.8	1.0

Table 2: Boundaries of each variable considered during the sensitivity analysis of T_{ij} .

Given the boundaries described in Table 2, the first order and total Sobol indices were calculated using the Satteli sampler [78] on thermal images taken at the four positions during a sunny

day in Singapore (i.e., November 17, 2021). It means that the variation of T_{ij} with respect to variables was estimated from a number R of samples, such that:

$$R = N \cdot (2D + 2) \quad (25)$$

where $N = 2^{12}$ and $D = 7$. For each sample, T_{ij} was calculated at different times of the day and positions of the thermal camera. The mean indices over the four positions were reported as the sensitivity of each variable at different times.

2.5. Calibration in an outdoor environment

Estimates of the surface temperature provided by the FLIR A300 camera were calibrated with respect to measurements collected with contact surface sensors. Contact surface sensors were installed at three different positions, as shown in Figure 4. At Position A, one Heat Flux (HF) sensor and one temperature probe were placed at the surface of a window in Building B between December 2021 and March 2022. Both the HF sensors

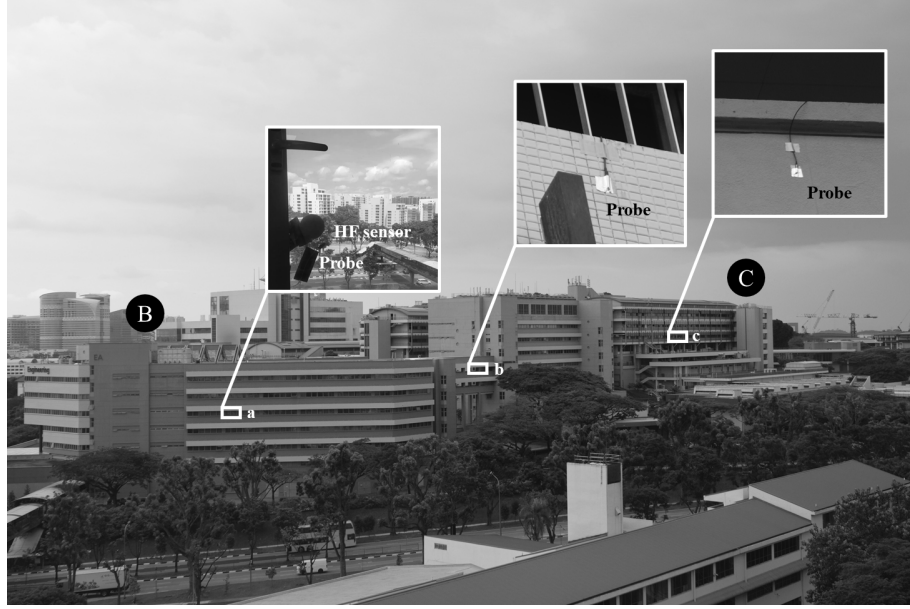


Figure 4: Positions where sensors were installed to measure the surface temperature and calibrate thermal images.

and the temperature probe were connected to a Hioki data logger. With this data logger, the surface temperature was measured every 3 seconds. Another type of datalogger, called UbiBot, was used to connect temperature two and three probes at Positions B and C, respectively. At these positions, the surface temperature was measured during April 2022 at a rate of one minute on concrete walls. During this period, the infrared camera was stopped at Position III and collected thermal images at a higher rate of one per 30 seconds. This choice was made to increase the number of estimates to compare with measurements over a shorter period.

The calibration of the FLIR A300 camera was manually performed by adjusting the parameters of Equation 21 till reaching a satisfactory agreement between estimates and measurements of the surface temperature. The agreement was evaluated with respect to the Root Mean Square Error (RMSE) and Mean Bias Error (MBE), which are expressed as:

$$RMSE = \sqrt{\frac{1}{N} \sum_{n=1}^N (T_S^n - T_{S,m}^n)^2} \quad (26)$$

$$MBE = \frac{1}{N} \sum_{n=1}^N (T_S^n - T_{S,m}^n) \quad (27)$$

where T_S^n is the surface temperature as evaluated from thermal images of the FLIR A300 camera at time $t = t_0 + n \cdot \Delta t$, and $T_{S,m}^n$ the surface temperature measured by contact surface sensors. The objective of the calibration was to reach an MBE as close as possible to 0 with the lowest RMSE. The RMSE and MBE were calculated with different Δt at Positions A-C. At Position A, the RMSE and MBE were evaluated with Δt equals 30 minutes. A smaller Δt of 5 minutes was used for computing the RMSE and MBE at Positions B and C. The reason is that measurements at Positions B and C were collected over a shorter period than at Position A.

2.6. Analysis of urban heat fluxes from thermal images

From thermal images collected by the observatory, it was possible to analyze heat fluxes within the urban canopy. It includes heat fluxes from façades of buildings A, B, C, and D, green areas at Positions I, II, III, and IV, and the traffic on the road observed at Position IV. Among these elements, some can be important contributors of UHIs while others might act as mitigators.

Building façades can considerably contribute to UHIs due to the heat they emit during the day and at night. The heat emitted by building façades, as well as by any built-up surface, depends on their orientation and material properties. For this reason, heat fluxes from façades of buildings A, B, C, and D were observed from different portions as shown in Figure 5. The façade of Building A consists of two steel walls and one glass wall, whose heat fluxes were assessed separately. Similarly, different portions were considered to observe heat fluxes from façades of buildings B, C, and D. Portions of buildings B and C are essentially walls consisting of the same material, that is, concrete, but with different orientations. Both steel and concrete walls can be observed on façades of the building D. Table 3 shows the thermal properties of building façades and the vegetation, which were defined from the literature. The distance from the observatory (d_{ij}) was measured from Google Earth. The thickness (Δx) of each built-up surface was assumed to be around 30 centimeters.

Figure 5 also shows the different portions of vegetation that were selected in thermal images to assess heat fluxes in the urban canopy. In contrast with building façades, the vegetation is normally considered a mitigator of UHIs. The reason is that the sensible heat emitted by the vegetation is normally lower than that released by built-up surfaces. Furthermore, the vegetation can reduce the outdoor air temperature through evapotranspiration, whose intensity can be evaluated from latent heat fluxes.

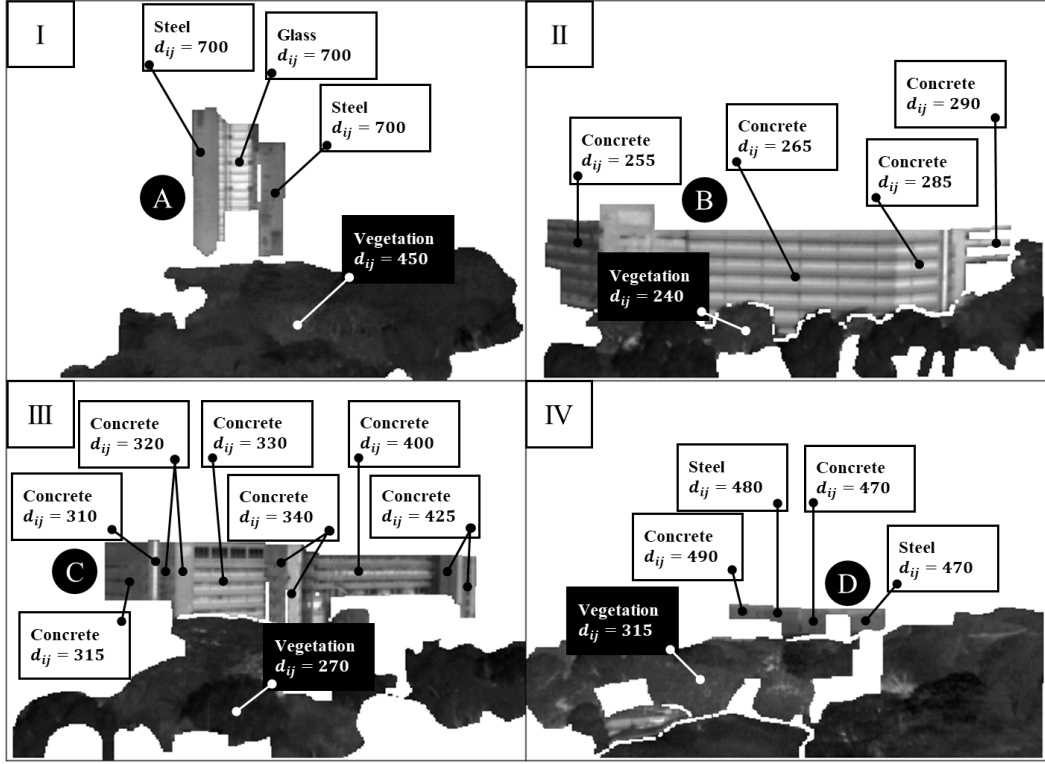


Figure 5: Built-up surfaces and green areas that were considered to analyze urban heat fluxes from the observatory.

Portion	Emissivity (0-1)	Density (kg/m ³)	Specific heat (J/kg·K)	Thickness (cm)	Thermal conductivity (W/m·K)	Reference
Steel	0.88	7940	507	10	-	[76]
Glass	0.93	2500	836	2.5	0.974	[79]
Concrete	0.90	2400	1180	30	0.62	[80]
						[81]
						[82]
						[83]
						[84]
						[85]
						[86]
Portion	Emissivity (0-1)	LAI (m ² /m ²)				Reference
Vegetation (Tropical trees)	0.98	4				[87]
						[88]

Table 3: Thermal properties of building façades and vegetation observed from the observatory at Positions I, II, III, and IV.

One heat flux, in particular, had to be measured with additional sensors, the conductive heat flux (Q_G). As illustrated in Figure 6, the conductive heat flux was measured at two different positions: one on the façade of Building A and another on the façade of Building C. On the façade of Building A, the interior surface temperature was measured with a temperature probe connected to a Hioki datalogger, while a UbiBot datalogger was used for measurements on the façade of Building C. The reason for choosing these two positions was to compare the full energy balance on glass and concrete walls. The conductive heat flux

through a glass wall should be higher than this measured on a concrete wall, and thus, it has different implications on the building energy consumption and UHIs.

As illustrated in Figure 7, a portion of a road at Position IV was selected in thermal images to evaluate the anthropogenic heat flux from traffic. Over this portion, it was assumed that only one car could be detected between two thermal images U_R^{n+1} and U_R^n . One car is detected if the peak value of $|U_R^{n+1} - U_R^n|$ is higher than a certain threshold (τ). It means that the function f

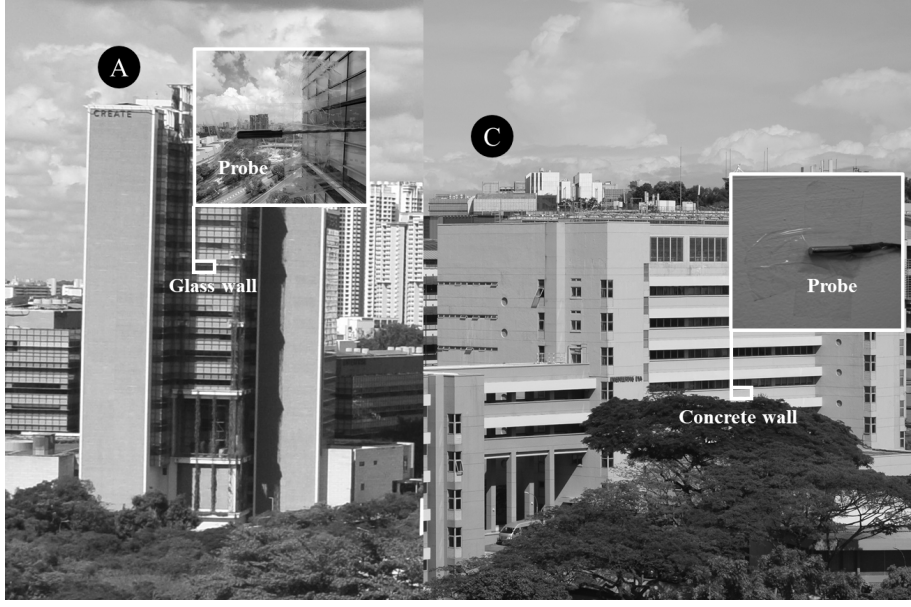


Figure 6: Positions where conductive heat fluxes (Q_G) were measured with contact surface sensors.

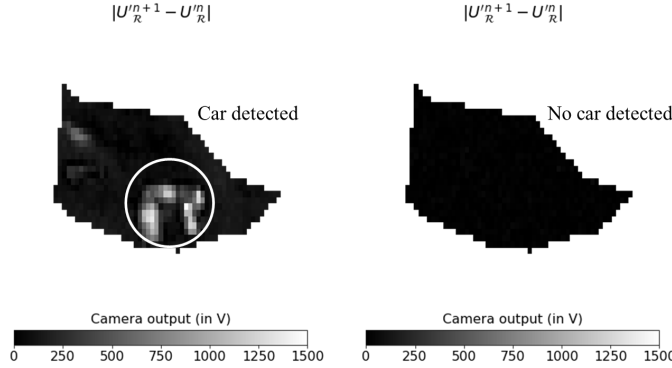


Figure 7: Car detection in a portion of a road at Position IV.

in Equation 17 is formulated as:

$$f(|U_{\mathcal{R}}^{n+1} - U_{\mathcal{R}}^n|) = \begin{cases} 1 & \text{if } \max |U_{\mathcal{R}}^{n+1} - U_{\mathcal{R}}^n| \geq \tau \\ 0 & \text{otherwise} \end{cases} \quad (28)$$

The value of τ corresponds to the highest magnitude of the noise that is contained in a thermal image. Regarding the portion of the road at Position IV, the highest magnitude of the noise, that is τ , was approximated as 150 Volts based on observations made on various thermal images collected by the observatory.

3. Results and discussions

3.1. Sensitivity analysis and calibration

Figure 8 shows the sensitivity of variables expressed in Equation 22 to estimate T_{ij} from the observatory. It appears that ε_{ij} , T_{sky} , T^{win} , and τ^{win} are more sensitive around 10 am and 3 pm than the rest of the day. At the observation site, 10 am, and 3 pm corresponds to instants when building façades are exposed to intense solar radiations. Consequently, it is implied that the solar exposure of building façades being observed affects the

sensitivity of some variables. In contrast, T_{air} seems to be more sensitive when building façades are not exposed to intense solar radiation. ϕ and d_{ij} look to be more sensitive around 10 am and 3 pm when their interaction with other variables is ignored but behave like T_{air} otherwise. This observation is explained from the fact that ϕ and d_{ij} strongly interact with T_{air} when calculating τ_{ij}^{atm} . Finally, τ^{win} appears to be the least sensitive variable to estimate T_{ij} .

Due to the sensitivity of some variables expressed in Equation 22, it was important to validate or calibrate estimates of T_{ij} with respect to some measurements. As explained in Section 2.5, measurements of the surface temperature were taken with contact surface sensors at three different positions (A-C). The RMSE and MBE obtained after calibration at these three different positions are shown in Table 4. At the three positions, it was possible to achieve an RMSE below 2 degrees Celsius and an MBE below ± 1 degree Celsius.

Constant	Original parameters	Calibrated parameters
b	1396.6000	1425.0000
f	1.0000	1.0000
O	-6303.0000	-9550.0000
r_1	14911.1846	14911.1850
r_2	0.0108	0.0120
Position	RMSE (in °C)	MBE (in °C)
a	1.24	-0.21
b	1.69	0.91
c	1.00	0.55

Table 4: Parameters resulting from the calibration of the FLIR A300 camera.

Figure 9 shows a comparison between estimates and measurements of the surface temperature after calibration at Positions A-C. At Position A, most underestimates seem to occur at night,

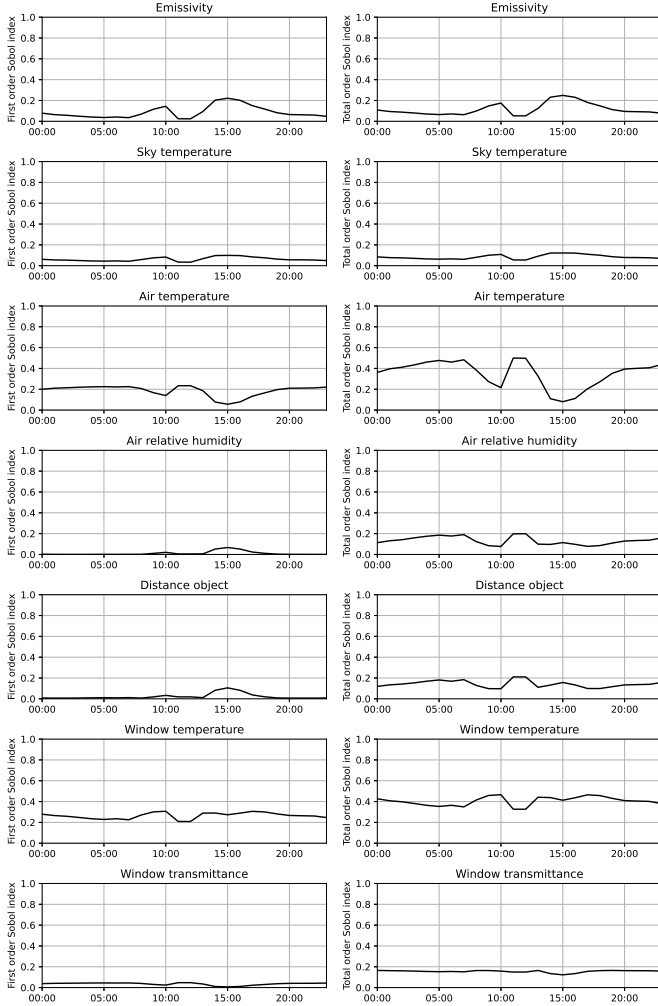


Figure 8: First order and total Sobol indexes of variables expressed in Equation 22 to obtain T_{ij} .

which might be due to the fact that the actual emissivity of the glass is slightly different from the one considered when estimating the surface temperature. In contrast, during the day, the surface temperature estimated from thermal images looks to be higher than this measured by contact sensors, in particular at Position B. A possible explanation is that the surface temperature measured by a contact sensor can be lower than the actual one as it needs to be fixed with tape on a wall. The tape may generate a small shadow effect around the temperature probe; and thus, create a cooler zone than its surroundings that are directly exposed to the sun.

3.2. Assessment of urban heat fluxes

After validating T_{ij} at different positions observed from the observatory, the surface temperature of building façades and vegetation described in Figure 5 were assessed using Equation 6. From the result shown in Figure 10, it appears that façades of buildings A, B, C, and D are hotter than vegetation over a typical day between November 2021 and March 2022. Among the façades, the one of Building A seems to be the hottest, in particular between 2 pm and 5 pm when highly exposed to the sun.

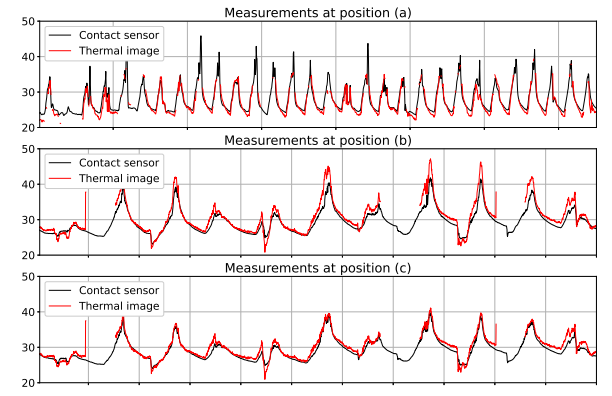


Figure 9: Comparison between estimates and measurements of the surface temperature after calibration of the A300 infrared camera when installed on the observatory.

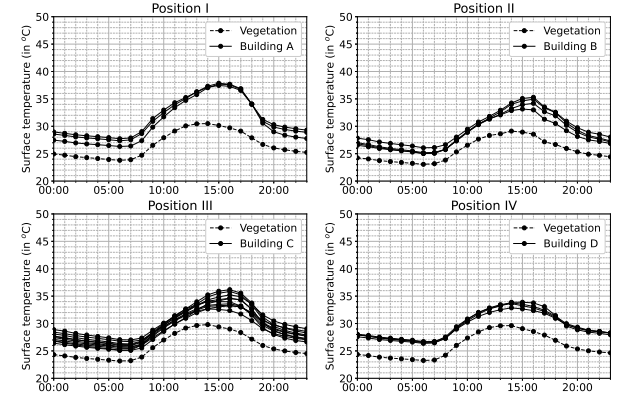


Figure 10: Daily average surface temperature of building façades A, B, C, and D in comparison to green areas at Positions I, II, III, and IV between November 2021 and March 2022.

A similar peak in the surface temperature can be observed on façades of Buildings B and C but at a lower magnitude than the façade of Building A. In contrast, no peak is observed between 2 pm and 5 pm on façades of Building D.

Results illustrated in Figures 10 imply that a typical high-rise office building in Singapore can potentially be an important contributor to UHIs in comparison to other buildings. However, the surface temperature alone does not determine the exact contribution of a building or other element to UHIs. The contribution to UHIs highly depends on how much heat penetrates into the building and how much is emitted towards the outdoor environment. For this reason, it was decided to analyze the various heat fluxes of building façades and vegetation at Positions I, II, III, and IV.

Sensible heat fluxes from building façades A, B, C, and D are shown in Figure 11. From this result, it appears building façades emit considerably more sensible heat than vegetation.

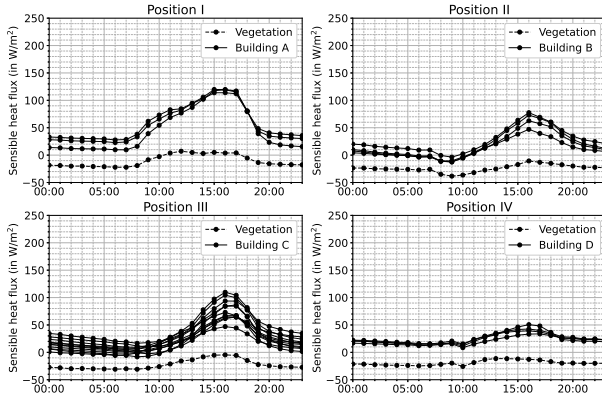


Figure 11: Daily average sensible heat flux of the façades of Buildings A, B, C, and D in comparison to green areas at Positions I, II, III, and IV between November 2021 and March 2022.

At the four positions, the sensible heat flux of vegetation seems to be relatively constant and always lower than this of building façades. The sensible heat emitted by buildings looks to be particularly intense during the day in comparison to the night. This observation is explained by the fact that the difference between the surface temperature of a building façade and the outdoor air temperature is usually higher during the day than at night. However, [66] reported that the temperature difference between the outdoor air and a building façade could be lower during a short period between 7 am and 1 pm than at night. This situation happens when the building façade is not highly exposed to the Sun at the beginning of the day, which appears to be the case for façades of Buildings B and C.

Besides sensible heat fluxes, the net-heat storage is another important aspect to observe for understanding the causes of UHIs. As theorized by [89], UHIs are essentially caused by the heat absorbed by built-up surfaces during the day, which is then released at night. This theory seems to be confirmed by results shown in Figure 12. In comparison to the vegetation, building façades accumulate a considerable amount of heat between 6 am and 3 pm. The accumulated heat appears to be then released at a high rate between 4 pm and 8 pm and at a lower one over the night. The high rate of heat loss by building façades partially coincides with intense sensible heat fluxes observed between 2 pm and 5 pm in Figure 11. Another reason is certainly the increase of the net-longwave radiation from building façades when their exposure to the Sun decreases.

To affirm that the heat loss between 4 pm and 8 pm is due to an augmentation of the heat emitted by longwave radiation, it would have been required to install a system for measuring the net-all wave radiation in the observatory. Despite this limitation, some assumptions can be made from data collected by the AWSN. According to the AWSN, the downward shortwave radiation considerably decreases from 2 pm on average over a typical day. From 5 pm, the sensible heat emitted by building façades also seems to decrease over time. The important heat loss observed between 4 pm and 8 pm can thus be the result of two phenomena.

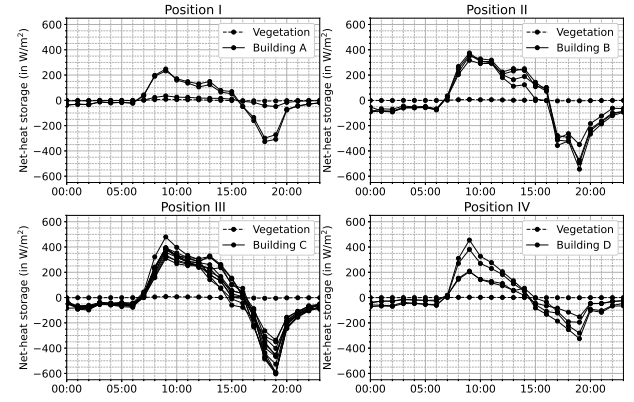


Figure 12: Daily average net-heat storage of the façades of Buildings A, B, C, and D in comparison to green areas at Positions I, II, III, and IV between November 2021 and March 2022.

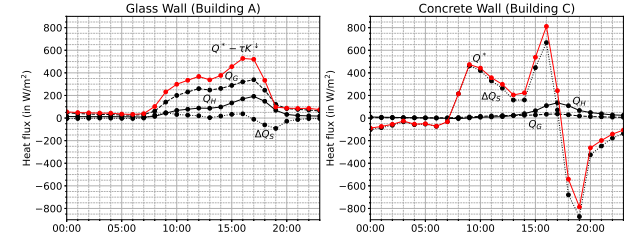


Figure 13: Daily average heat fluxes of the glass wall (Building A) and the concrete wall (Building C) during sunny days between February 2022 and March 2022.

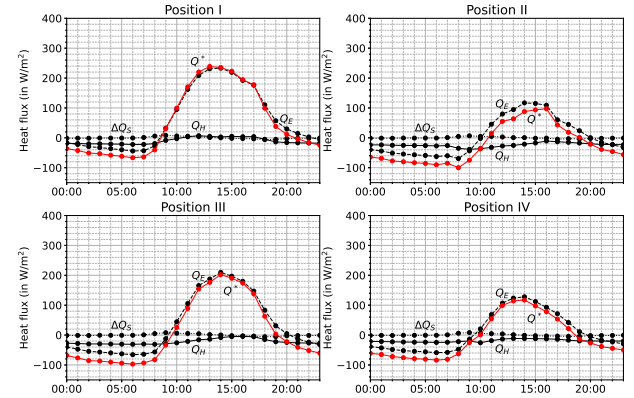


Figure 14: Daily average heat fluxes of trees at Positions I, II, III, and IV between November 2021 and March 2022.

One hypothesis could be an increase in the heat penetration into buildings by conduction through their façades. The other hypothesis is then that building façades lose heat between 4 pm and 8 pm because their radiative heat exchanges with the sky and their surrounding elements as simulated by [76].

Figure 13 shows all heat fluxes as measured from thermal

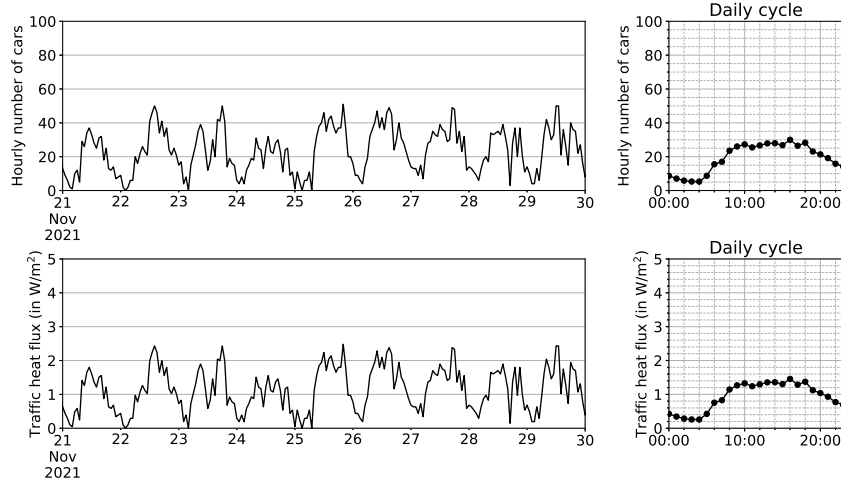


Figure 15: Number of cars and traffic heat flux on a portion of a road at Position IV over the month of November 2021.

images and contact surface sensors at points Buildings A and C. On the glass wall of Building A, the conductive heat flux (Q_G) appears to be relatively high, even at night. It implies that the small decrease in the net heat storage (ΔQ_S) between 5pm and 6pm is due to intense sensible and conductive heat fluxes in comparison to the net-all wave radiation (Q^*). The net-all wave radiation seems to remain positive on the glass wall all over a typical day, which means that more radiations are absorbed by the surface or transmitted into Building A than reflected or re-emitted into the outdoor environment. Therefore, it can be expected that high-rise and highly-glazed buildings contribute more to UHIs by waste heat releases caused by air-conditioning than the reflected or re-emitted radiations from the surface.

On the other hand, it is demonstrated in Figure 13 that re-emitted longwave radiations (L^\uparrow) from a concrete wall can be a serious contributor to UHIs, in particular at night. This observation is justified by the fact that the conductive heat flux (Q_G) seems to be relatively low through the concrete wall of Building C. Thus, it can be confirmed that negative values of the net-all wave radiation (Q^*) at night appear to be due to the outgoing longwave radiation from the concrete wall.

According to results shown in Figure 14, vegetation also emits more longwave radiations than it absorbs at night. However, the heat emitted by longwave radiations looks to be balanced by the sensible heat absorbed by the vegetation, which makes the net heat added into the outdoor environment negligible. While the vegetation does not seem to add or extract much heat from the outdoor environment at night, it appears to generate a visible net-cooling effect during the day. The net-cooling effect is largely due to the fact that the vegetation emits little sensible heat and releases a considerable amount of latent heat. This observation implies that vegetation refreshes the outdoor environment by evapotranspiration more than warming it by convection from its surface. At Positions II, III, and IV, it seems that vegetation can even directly absorb heat from the outdoor environment by convection during the day, creating a more significant cooling effect.

Apart from the assessment of the heat emitted and stored by building façades and vegetation at the neighborhood scale, another major novelty of this study was to estimate the heat emitted by an anthropogenic heat source like traffic directly from thermal images. Figure 15 shows the traffic intensity and heat fluxes over the month of November 2021 as estimated using the Equations 18 and 19, respectively. It demonstrates that the traffic is heavier during the day than at night, with two important peaks at 4 pm and 6 pm. The magnitude of traffic heat fluxes does not go beyond 3 watts per square meter, which is a relatively low value in comparison to other urban heat fluxes. Nevertheless, it is important to remember that the traffic heat flux illustrated in Figure 15 was calculated for a portion of a road only. If it had been possible to detect the traffic over a larger portion of the road from the observatory, the magnitude of heat fluxes could have been superior to 3 watts per square meter.

4. Conclusions

This study described a method to analyze urban heat flux at the neighborhood scale using thermal images and weather data. While thermal images were obtained from a rooftop observatory, weather data were collected from an AWSN. From these two data sources, it was possible to assess the heat emitted and stored by building façades and green areas within a university campus in Singapore. In addition, traffic heat fluxes were estimated based on a sequence of thermal images only.

Before analyzing urban heat fluxes on the university campus, a sensitivity analysis was performed on the method used to estimate the surface temperature of elements observed from the infrared camera installed in the observatory. The analysis revealed that some variables are more sensitive during the day while others are at night. Among the sensitive variables, there are the outdoor air temperature and relative humidity, which can be measured from the AWSN. Other sensitive variables, however, had to be approximated either from values reported in the literature or from additional instruments. These variables include the emissivity of elements observed from the infrared camera,

their distance from the observatory, and the surface temperature of the window protecting the infrared camera in a housing. To improve the accuracy of thermal images collected by an infrared, these three variables should be directly measured from devices integrated into the observatory. For example, studies proposed methods to measure the emissivity of different surfaces from satellite [90, 91, 92]. Another instrument to integrate with the observatory could be a PT100 contact sensor to measure the surface temperature of the window as in the Kipp & Zonen CNR4 radiometer.

After the sensitivity analysis, some parameters used to estimate the surface temperature was calibrated against measurements in an outdoor environment. With calibrated parameters, it was possible to achieve an RMSE below 2 degrees Celsius and an MBE below ± 1 degree Celsius between measurements and estimates. The probability that the discrepancy between measurements and estimates is higher than 2.5 degrees Celsius is relatively low. However, this accuracy was achieved from measurements of the surface temperature collected by a few contact sensors installed on opaque surfaces. In the future, it would be recommended to calibrate thermal images with more contact sensors which could also be installed in green areas.

Besides the sensitivity analysis and calibration, the study shows that it is possible to observe contributors to UHIs at the neighborhood scale from thermal images collected by a rooftop observatory and weather data recorded by an AWSN. Among the contributors, it is possible to see the sensible heat emitted by building façades during the day. Knowing the conduction through the building façades, thermal images alone can be used to infer their net-longwave radiation at night. Because of the nighttime net-longwave radiation, concrete walls seem to be an important contributor to UHIs. In contrast, glass walls appear to have lower net radiation at nighttime according to heat fluxes assessed from the rooftop observatory. However, they have lower insulation which can potentially cause considerable heat releases due to the use of air conditioning. The heat released by an HVAC system is a contributor to UHIs that can hardly be assessed from thermal images at the neighborhood scale. [67] showed that their location could be detected, but not their magnitude.

Although the contribution of HVAC systems to UHIs at the neighborhood scale remains an aspect to be further explored in the future, this study proved that thermal images could be used to detect cars on the road as well as the magnitude of the heat they release. The method should be used on several portions of a road to have a better understanding of the total contribution of traffic on UHIs.

Apart from contributors of UHIs, the effect of vegetation on the outdoor environment at the neighborhood scale can also be observed from thermal images and weather data. The vegetation appears to emit significantly more latent than sensible heat during the day, which enables it to cool the outdoor environment. At night, the vegetation does not look to warm or cool the outdoor environment. Although these observations were theorized a long time ago by [93], it is the first time they are made from thermal images and weather data collected at the neighborhood scale. Despite this achievement, one limitation is that the vegetation was observed as a whole to see how consider-

ably building façades might contribute to UHIs. In the future, it would be recommended to study heat fluxes from different types of vegetation and see which ones might be better mitigators to UHIs.

Acknowledgement

This research is supported by the National Research Foundation and the Prime Minister’s Office of Singapore under its Campus for Research Excellence and Technological Enterprise (CREATE) program. It was funded through a grant to the Berkeley Education Alliance for Research in Singapore (BEARS) for the Singapore-Berkeley Building Efficiency and Sustainability in the Tropics (SinBerBEST) program. BEARS was established by the University of California, Berkeley, as a center for intellectual excellence in research and education in Singapore.

The University Campus Infrastructure of the National University of Singapore also provided great assistance to this research by sharing data obtained during the Virtual Campus project.

References

- [1] H. Ritchie and M. Roser. Urbanization. *Our world in data*, 2018.
- [2] S. Campbell, T. A. Remenyi, C. J. White, and F. H. Johnston. Heatwave and health impact research: A global review. *Health & place*, 53:210–218, 2018.
- [3] H. Bahi, H. Mastouri, and H. Radoine. Review of methods for retrieving urban heat islands. *Materials Today: Proceedings*, 27:3004–3009, 2020.
- [4] J. C. Price. Assessment of the urban heat island effect through the use of satellite data. *Monthly Weather Review*, 107(11):1554–1557, 1979.
- [5] M. Roth, T. R. Oke, and W. J. Emery. Satellite-derived urban heat islands from three coastal cities and the utilization of such data in urban climatology. *International Journal of Remote Sensing*, 10(11):1699–1720, 1989.
- [6] W. Wang, K. Liu, R. Tang, and S. Wang. Remote sensing image-based analysis of the urban heat island effect in shenzhen, china. *Physics and Chemistry of the Earth, Parts A/B/C*, 110:168–175, 2019.
- [7] Y.-H. Kim and J.-J. Baik. Spatial and temporal structure of the urban heat island in Seoul. *Journal of Applied Meteorology and Climatology*, 44(5):591–605, 2005.
- [8] J. Tan, Y. Zheng, X. Tang, C. Guo, L. Li, G. Song, X. Zhen, D. Yuan, A. J. Kalkstein, F. Li, et al. The urban heat island and its impact on heat waves and human health in Shanghai. *International journal of biometeorology*, 54(1):75–84, 2010.
- [9] D. Wolters and T. Brandsma. Estimating the urban heat island in residential areas in the Netherlands using observations by weather amateurs. *Journal of Applied Meteorology and Climatology*, 51(4):711–721, 2012.
- [10] E. L. Warren, D. T. Young, L. Chapman, C. Muller, C. S. B. Grimmond, and X.-M. Cai. The Birmingham Urban Climate Laboratory—A high density, urban meteorological dataset, from 2012–2014. *Scientific data*, 3(1):1–8, 2016.
- [11] F. Meier, D. Fenner, T. Grassmann, M. Otto, and D. Scherer. Crowdsourcing air temperature from citizen weather stations for urban climate research. *Urban Climate*, 19:170–191, 2017.
- [12] P. Konstantinov, M. Varentsov, and I. Esau. A high density urban temperature network deployed in several cities of Eurasian Arctic. *Environmental Research Letters*, 13(7):075007, 2018.
- [13] C. D. W. Rogers, A. J. E. Gallant, and N. J. Tapper. Is the urban heat island exacerbated during heatwaves in southern Australian cities? *Theoretical and Applied Climatology*, 137(1):441–457, 2019.
- [14] F. Meng, J. Guo, G. Ren, L. Zhang, and R. Zhang. Impact of urban heat island on the variation of heating loads in residential and office buildings in Tianjin. *Energy and Buildings*, 226:110357, 2020.
- [15] V. D. P. R. Da Silva, P. V. De Azevedo, R. S. Brito, and J. H. B. Da Cunha Campos. Evaluating the urban climate of a typically tropical city of northeastern Brazil. *Environmental monitoring and assessment*, 161(1):45–59, 2010.
- [16] L. W. A. Van Hove, C. M. J. Jacobs, B. G. Heusinkveld, J. A. Elbers, B. L. Van Driel, and A. A. M. Holtslag. Temporal and spatial variability of

urban heat island and thermal comfort within the Rotterdam agglomeration. *Building and Environment*, 83:91–103, 2015.

[17] C. K. C. Lam and J. Hang. Solar radiation intensity and outdoor thermal comfort in royal botanic garden Melbourne during heatwave conditions. *Procedia Engineering*, 205:3456–3462, 2017.

[18] G. Roshan, M. Moghbel, and S. Attia. Evaluating the wind cooling potential on outdoor thermal comfort in selected Iranian climate types. *Journal of Thermal Biology*, 92:102660, 2020.

[19] M. Szymanowski and M. Kryza. Local regression models for spatial interpolation of urban heat island—an example from Wrocław, SW poland. *Theoretical and applied climatology*, 108(1):53–71, 2012.

[20] P. Yang, G. Ren, and W. Liu. Spatial and temporal characteristics of Beijing urban heat island intensity. *Journal of applied meteorology and climatology*, 52(8):1803–1816, 2013.

[21] R. Bassett, X. Cai, L. Chapman, C. Heaviside, John E. Thorne, C. L. Muller, D. T. Young, and E. L. Warren. Observations of urban heat island advection from a high-density monitoring network. *Quarterly Journal of the Royal Meteorological Society*, 142(699):2434–2441, 2016.

[22] L. Chapman, C. Bell, and S. Bell. Can the crowdsourcing data paradigm take atmospheric science to a new level? a case study of the urban heat island of London quantified using Netatmo weather stations. *International Journal of Climatology*, 37(9):3597–3605, 2017.

[23] L. Liu, Y. Lin, J. Liu, L. Wang, D. Wang, T. Shui, X. Chen, and Q. Wu. Analysis of local-scale urban heat island characteristics using an integrated method of mobile measurement and GIS-based spatial interpolation. *Building and Environment*, 117:191–207, 2017.

[24] N. Yadav and C. Sharma. Spatial variations of intra-city urban heat island in megacity Delhi. *Sustainable cities and society*, 37:298–306, 2018.

[25] R. R. Shaker, Y. Altman, C. Deng, E. Vaz, and K. W. Forsythe. Investigating urban heat island through spatial analysis of New York City streetscapes. *Journal of cleaner production*, 233:972–992, 2019.

[26] S. Caluwaerts, R. Hamdi, S. Top, D. Lauwaet, J. Berckmans, D. Degrauwe, H. Dejonghe, K. De Ridder, R. De Troch, F. Duchêne, et al. The urban climate of Ghent, Belgium: A case study combining a high-accuracy monitoring network with numerical simulations. *Urban Climate*, 31:100565, 2020.

[27] Y. F. Lam, C.-W. Ong, M.-H. Wong, W.-F. Sin, and C.-W. Lo. Improvement of community monitoring network data for urban heat island investigation in Hong Kong. *Urban Climate*, 37:100852, 2021.

[28] F. Flores, M. Lillo, et al. Simple air temperature estimation method from MODIS satellite images on a regional scale. *Chilean Journal of Agricultural Research*, 70(3):436–445, 2010.

[29] M. Şahin. Modelling of air temperature using remote sensing and artificial neural network in Turkey. *Advances in space research*, 50(7):973–985, 2012.

[30] Itai Kloog, Alexandra Chudnovsky, Petros Kourakis, and Joel Schwartz. Temporal and spatial assessments of minimum air temperature using satellite surface temperature measurements in massachusetts, usa. *Science of the total environment*, 432:85–92, 2012.

[31] H. C. Ho, A. Knudby, P. Sirovyak, Y. Xu, M. Hodul, and S. B. Henderson. Mapping maximum urban air temperature on hot summer days. *Remote Sensing of Environment*, 154:38–45, 2014.

[32] I. Kloog, F. Nordio, B. A. Coull, and J. Schwartz. Predicting spatiotemporal mean air temperature using MODIS satellite surface temperature measurements across the Northeastern USA. *Remote sensing of environment*, 150:132–139, 2014.

[33] L. Hu, A. J. Monaghan, and N. A. Brunsell. Investigation of urban air temperature and humidity patterns during extreme heat conditions using satellite-derived data. *Journal of Applied Meteorology and Climatology*, 54(11):2245–2259, 2015.

[34] J. A. Azevedo, L. Chapman, and C. L. Muller. Quantifying the daytime and night-time urban heat island in Birmingham, UK: A comparison of satellite derived land surface temperature and high resolution air temperature observations. *Remote Sensing*, 8(2):153, 2016.

[35] D. Montaner-Fernández, L. Morales-Salinas, J. S. Rodriguez, L. Cárdenas-Jirón, A. Huete, G. Fuentes-Jaque, W. Pérez-Martínez, and J. Cabezas. Spatio-temporal variation of the urban heat island in Santiago, Chile during summers 2005–2017. *Remote Sensing*, 12(20):3345, 2020.

[36] W. Zhou, S. Ji, T.-H. Chen, Y. Hou, and K. Zhang. The 2011 heat wave in Greater Houston: Effects of land use on temperature. *Environmental research*, 135:81–87, 2014.

[37] Y. Y. Lee, J. T. Kim, and G. Y. Yun. The neural network predictive model for heat island intensity in Seoul. *Energy and Buildings*, 110:353–361, 2016.

[38] Y. Shi, L. Katschner, and E. Ng. Modelling the fine-scale spatiotemporal pattern of urban heat island effect using land use regression approach in a megacity. *Science of the Total Environment*, 618:891–904, 2018.

[39] Y.-C. Chen, Y.-J. Liao, C.-K. Yao, T. Honjo, C.-K. Wang, and T.-P. Lin. The application of a high-density street-level air temperature observation network (HiSAN): The relationship between air temperature, urban development, and geographic features. *Science of the Total Environment*, 685:710–722, 2019.

[40] M. Burger, M. Gubler, A. Heinimann, and S. Brönnimann. Modelling the spatial pattern of heatwaves in the city of Bern using a land use regression approach. *Urban climate*, 38:100885, 2021.

[41] Y. Ma, O. Tsukamoto, H. Ishikawa, Z. Su, M. Menenti, J. Wang, and J. Wen. Determination of regional land surface heat flux densities over heterogeneous landscape of heife integrating satellite remote sensing with field observations. *Journal of the Meteorological Society of Japan. Ser. II*, 80(3):485–501, 2002.

[42] N. Chrysoulakis. Estimation of the all-wave Net Radiation Balance in Urban Environment with the combined use of Terra/ASTER multispectral imagery and in-situ spatial data. *J. Geophys. Res.*, 108(D18):4582, 2003.

[43] G. Bisht, V. Venturini, S. Islam, and L. E. Jiang. Estimation of the net radiation using MODIS (Moderate Resolution Imaging Spectroradiometer) data for clear sky days. *Remote sensing of environment*, 97(1):52–67, 2005.

[44] K. Wang, Z. Wan, P. Wang, M. Sparrow, J. Liu, X. Zhou, and S. Hagiwara. Estimation of surface long wave radiation and broadband emissivity using Moderate Resolution Imaging Spectroradiometer (MODIS) land surface temperature/emissivity products. *Journal of Geophysical Research: Atmospheres*, 110(D11), 2005.

[45] B. Tang and Z.-L. Li. Estimation of instantaneous net surface longwave radiation from MODIS cloud-free data. *Remote Sensing of Environment*, 112(9):3482–3492, 2008.

[46] G. Bisht and Rafael L. Bras. Estimation of net radiation from the MODIS data under all sky conditions: Southern Great Plains case study. *Remote Sensing of Environment*, 114(7):1522–1534, 2010.

[47] H. Wu, X. Zhang, S. Liang, H. Yang, and G. Zhou. Estimation of clear-sky land surface longwave radiation from modis data products by merging multiple models. *Journal of Geophysical Research: Atmospheres*, 117(D22), 2012.

[48] B. Qin, B. Cao, Z. Li, H. and Bian, T. Hu, Y. Du, Y. Yang, Q. Xiao, and Q. Liu. Evaluation of six high-spatial resolution clear-sky surface upward longwave radiation estimation methods with MODIS. *Remote Sensing*, 12(11):1834, 2020.

[49] J. M. Norman, W. P. Kustas, J. H. Prueger, and G. R. Diak. Surface flux estimation using radiometric temperature: A dual-temperature-difference method to minimize measurement errors. *Water Resources Research*, 36(8):2263–2274, 2000.

[50] A. N. French, T. J. Schmugge, W. P. Kustas, K. L. Brubaker, and J. Prueger. Surface energy fluxes over El Reno, Oklahoma, using high-resolution remotely sensed data. *Water resources research*, 39(6), 2003.

[51] Y. Liu, G. Shintaro, D. Zhuang, and W. Kuang. Urban surface heat fluxes infrared remote sensing inversion and their relationship with land use types. *Journal of Geographical Sciences*, 22(4):699–715, 2012.

[52] G. Rios and P. Ramamurthy. A novel model to estimate sensible heat fluxes in urban areas using satellite-derived data. *Remote Sensing of Environment*, 270:112880, 2022.

[53] S. Kato and Y. Yamaguchi. Analysis of urban heat-island effect using ASTER and ETM+ Data: Separation of anthropogenic heat discharge and natural heat radiation from sensible heat flux. *Remote Sensing of Environment*, 99(1-2):44–54, 2005.

[54] S. Kato and Y. Yamaguchi. Estimation of storage heat flux in an urban area using ASTER data. *Remote Sensing of Environment*, 110(1):1–17, 2007.

[55] W. Xu, M. J. Wooster, and C. S. B. Grimmond. Modelling of urban sensible heat flux at multiple spatial scales: A demonstration using airborne hyperspectral imagery of Shanghai and a temperature–emissivity separation approach. *Remote Sensing of Environment*, 112(9):3493–3510, 2008.

[56] Q. Weng, X. Hu, D. A. Quattrochi, and H. Liu. Assessing intra-urban

surface energy fluxes using remotely sensed ASTER imagery and routine meteorological data: A case study in indianapolis, USA. *IEEE Journal of Selected Topics in Applied Earth Observations and Remote Sensing*, 7(10):4046–4057, 2013.

[57] S. D. Chakraborty, Y. Kant, and D. Mitra. Assessment of land surface temperature and heat fluxes over Delhi using remote sensing data. *Journal of environmental management*, 148:143–152, 2015.

[58] S. Chen and D. Hu. Parameterizing anthropogenic heat flux with an energy-consumption inventory and multi-source remote sensing data. *Remote Sensing*, 9(11):1165, 2017.

[59] C. Feigenwinter, R. Vogt, E. Parlow, F. Lindberg, M. Marconcini, F. Del Frate, and N. Chrysoulakis. Spatial distribution of sensible and latent heat flux in the city of basel (switzerland). *IEEE Journal of Selected Topics in Applied Earth Observations and Remote Sensing*, 11(8):2717–2723, 2018.

[60] N. Chrysoulakis, S. Grimmond, C. Feigenwinter, F. Lindberg, J.-P. Gastellu-Etchegorry, M. Marconcini, Z. Mitroka, S. Stagakis, B. Crawford, F. Olofson, et al. Urban energy exchanges monitoring from space. *Scientific reports*, 8(1):1–8, 2018.

[61] A. Oliveira, A. Lopes, S. Niza, and A. Soares. An urban energy balance-guided machine learning approach for synthetic nocturnal surface Urban Heat Island prediction: A heatwave event in Naples. *Science of the total environment*, 805:150130, 2022.

[62] J. Richters, F. Meier, and D. Scherer. Analysis of long-wave radiation from urban facets derived from time-sequential thermography (TST) and 3D city model. In *7th International Conference on Urban Climate*, volume 29, 2009.

[63] W. Morrison, T. Yin, N. Lauret, J. Guilleux, S. Kotthaus, J.-P. Gastellu-Etchegorry, L. Norford, and S. Grimmond. Atmospheric and emissivity corrections for ground-based thermography using 3D radiative transfer modelling. *Remote Sensing of Environment*, 237:111524, 2020.

[64] W. Morrison, S. Kotthaus, and S. Grimmond. Urban surface temperature observations from ground-based thermography: intra-and inter-facet variability. *Urban Climate*, 35:100748, 2021.

[65] J. F. C. Sham, T. Y. Lo, and S. A. Memon. Verification and application of continuous surface temperature monitoring technique for investigation of nocturnal sensible heat release characteristics by building fabrics. *Energy and Buildings*, 53:108–116, 2012.

[66] A. Hoyano, K. Asano, and T. Kanamaru. Analysis of the sensible heat flux from the exterior surface of buildings using time sequential thermography. *Atmospheric Environment*, 33(24–25):3941–3951, 1999.

[67] G. Dobler, F. B. Bianco, M. S. Sharma, A. Karpf, J. Baur, M. Ghandehari, J. Wurtele, and S. E. Koonin. The Urban Observatory: A Multi-Modal Imaging Platform for the Study of Dynamics in Complex Urban Systems. *Remote Sensing*, 13(8):1426, 2021.

[68] V. Masson. A physically-based scheme for the urban energy budget in atmospheric models. *Boundary-layer meteorology*, 94(3):357–397, 2000.

[69] Sang-Hyun Lee and Soon-Ung Park. A vegetated urban canopy model for meteorological and environmental modelling. *Boundary-Layer Meteorology*, 126(1):73–102, 2008.

[70] Y. Kikegawa, Y. Genchi, H. Yoshikado, and H. Kondo. Development of a numerical simulation system toward comprehensive assessments of urban warming countermeasures including their impacts upon the urban buildings' energy-demands. *Applied Energy*, 76(4):449–466, 2003.

[71] C. S. B. Grimmond. The suburban energy balance: Methodological considerations and results for a mid-latitude west coast city under winter and spring conditions. *International Journal of Climatology*, 12(5):481–497, 1992.

[72] Z. Yu, S. Chen, N. H. Wong, M. Ignatius, J. Deng, Y. He, and D. J. C. Hii. Dependence between urban morphology and outdoor air temperature: A tropical campus study using random forests algorithm. *Sustainable Cities and Society*, 61:102200, 2020.

[73] M. Waldemar and D. Klecha. Modeling of atmospheric transmission coefficient in infrared for thermovision measurements. In *Proceedings of the Sensor*, pages 903–907, 2015.

[74] I. M. Sobol. Global sensitivity indices for nonlinear mathematical models and their Monte Carlo estimates. *Mathematics and computers in simulation*, 55(1–3):271–280, 2001.

[75] P. E. Osborne and T. Alvares-Sanches. Quantifying how landscape composition and configuration affect urban land surface temperatures using machine learning and neural landscapes. *Computers, Environment and Urban Systems*, 76:80–90, 2019.

[76] M. Miguel, W. N. Hien, I. Marcel, H. D. J. Chung, H. Yueer, Y. Zhonqi, D. Ji-Yu, S. V. Raghavan, and N. N. Son. A physically-based model of interactions between a building and its outdoor conditions at the urban microscale. *Energy and Buildings*, 237:110788, 2021.

[77] MSS. Historical Daily Records, 2022.

[78] A. Saltelli, P. Annoni, I. Azzini, F. Campolongo, M. Ratto, and S. Tarantola. Variance based sensitivity analysis of model output. Design and estimator for the total sensitivity index. *Computer physics communications*, 181(2):259–270, 2010.

[79] G. Meneghetti, M. Ricotta, and B. Atzori. A synthesis of the push-pull fatigue behaviour of plain and notched stainless steel specimens by using the specific heat loss. *Fatigue & Fracture of Engineering Materials & Structures*, 36(12):1306–1322, 2013.

[80] R. Raman and A. Thakur. Thermal emissivity of materials. *Applied Energy*, 12(3):205–220, 1982.

[81] H. N. Ritland. Density phenomena in the transformation range of a borosilicate crown glass. *Journal of the American Ceramic Society*, 37(8):370–377, 1954.

[82] D. E. Sharp and L. B. Ginther. Effect of composition and temperature on the specific heat of glass. *Journal of the American Ceramic Society*, 34(9):260–271, 1951.

[83] X. Wang, S. Shan, S. Q. Shi, Y. Zhang, L. Cai, and L. M. Smith. Optically transparent bamboo with high strength and low thermal conductivity. *ACS Applied Materials & Interfaces*, 13(1):1662–1669, 2020.

[84] S. Ifat. Relation between density and compressive strength of hardened concrete. *Concrete Research Letters*, 6(4):182–189, 2015.

[85] G. De Schutter and L. Taerwe. Specific heat and thermal diffusivity of hardening concrete. *Magazine of Concrete research*, 47(172):203–208, 1995.

[86] K.-H. Kim, S.-E. Jeon, J.-K. Kim, and S. Yang. An experimental study on thermal conductivity of concrete. *Cement and concrete research*, 33(3):363–371, 2003.

[87] A. Olioso. Simulating the relationship between thermal emissivity and the normalized difference vegetation index. *International Journal of Remote Sensing*, 16(16):3211–3216, 1995.

[88] S. Ganguly, A. Samanta, M. A. Schull, Nikolay V. Shabanov, C. Milesi, R. R. Nemani, Y. Knyazikhin, and R. B. Myneni. Generating vegetation leaf area index Earth system data record from multiple sensors. Part 2: Implementation, analysis and validation. *Remote Sensing of Environment*, 112(12):4318–4332, 2008.

[89] T. R. Oke. Canyon geometry and the nocturnal urban heat island: comparison of scale model and field observations. *Journal of climatology*, 1(3):237–254, 1981.

[90] K. Ogawa, T. Schmugge, F. Jacob, and A. French. Estimation of broadband land surface emissivity from multi-spectral thermal infrared remote sensing. *Agronomie*, 22(6):695–696, 2002.

[91] Beatriz Ribeiro Da Luz and James K Crowley. Spectral reflectance and emissivity features of broad leaf plants: Prospects for remote sensing in the thermal infrared (8.0–14.0 μ m). *Remote sensing of environment*, 109(4):393–405, 2007.

[92] K. Ogawa, T. Schmugge, and S. Rokugawa. Estimating broadband emissivity of arid regions and its seasonal variations using thermal infrared remote sensing. *IEEE Transactions on Geoscience and Remote Sensing*, 46(2):334–343, 2008.

[93] T. R. Oke and J. H. McCaughey. Suburban-rural energy balance comparisons for vancouver, bc: an extreme case? *Boundary-Layer Meteorology*, 26(4):337–354, 1983.